Pulmonary Circulation

WILEY

PVRi Pulmonary Circulation Open Access

RESEARCH ARTICLE OPEN ACCESS

An Unsupervised Approach to Derive Right Ventricular Pressure–Volume Loop Phenotypes in Pulmonary Hypertension

Nikita Sivakumar[1,2] | Cindy Zhang[1,2] | Connie Chang-Chien[1] | Pan Gu[1] | Yikun Li[1,2] | Yi Yang[1] | Darin Rosen[3] | Tijana Tuhy[3] | Ilton M. Cubero Salazar[4] | Matthew Kauffman[3] | Rachel L. Damico[3] | Casey Overby Taylor[1,2,5] | Joseph L. Greenstein[1,2] | Steven Hsu[4] | Paul M. Hassoun[3] | Catherine E. Simpson[3]

[1]Institute for Computational Medicine, Johns Hopkins University, Baltimore, Maryland, USA | [2]Department of Biomedical Engineering, Johns Hopkins University, Baltimore, Maryland, USA | [3]Division of Pulmonary and Critical Care Medicine, Baltimore, Maryland, USA | [4]Division of Cardiology, Johns Hopkins University School of Medicine, Baltimore, Maryland, USA | [5]Division of General Internal Medicine, Johns Hopkins University School of Medicine, Baltimore, Maryland, USA

Correspondence: Catherine E. Simpson (Catherine.simpson@jhmi.edu)

Received: 24 September 2024 | **Revised:** 29 January 2025 | **Accepted:** 7 February 2025

Funding: This work was supported by K23HL146889, NIH 1L30HL165545-01, NIH 5T32HL007227-47, NIH/NHLBI K23HL153781, and R01HL114910.

Keywords: cardiac resonance imaging | right heart catheterization | right ventricular-pulmonary arterial coupling | unsupervised clustering

ABSTRACT

Although right ventricle (RV) dysfunction drives clinical worsening in pulmonary hypertension (PH), information about RV function has not been well integrated in PH risk assessment. The gold standard for assessing RV function and ventriculo-arterial coupling is the construction of multi-beat pressure–volume (PV) loops. PV loops are technically challenging to acquire and not feasible for routine clinical use. Therefore, we aimed to map standard clinically available measurements to emergent PV loop phenotypes. One hundred and one patients with suspected PH underwent right heart catheterization (RHC) with exercise, multi-beat PV loop measurement, and same-day cardiac magnetic resonance imaging (CMR). We applied unsupervised *k*-means clustering on 10 PV loop metrics to obtain three patient groups with unique RV functional phenotypes and times to clinical worsening. We integrated RHC and CMR measurements to train a random forest classifier that predicts the PV loop patient group with high discrimination (AUC = 0.93). The most informative variable for PV loop phenotype prediction was exercise mean pulmonary arterial pressure (mPAP). Distinct and clinically meaningful PV loop phenotypes exist that can be predicted using clinically accessible hemodynamic and RV-centric measurements. Exercise mPAP may inform RV pressure–volume relationships.

1 | Introduction

Pulmonary hypertension (PH) is an incurable disease of the pulmonary vasculature that affects over 100 million individuals worldwide and remains a challenging condition to diagnose and treat [1]. Elevated pulmonary pressures increase the load imposed on the right ventricle (RV), and if untreated, result in progressive RV remodeling and dysfunction. Prior work has shown that the ability (or inability) of the RV to adaptively remodel in response to increased load is the main determinant of PH prognosis [2–6]. However, noninvasively measuring RV function is clinically challenging due to the unique structure and orientation of the RV. Current clinical risk assessment tools, such as the REVEAL risk score [7, 8] or the COMPERA risk score [9], do not integrate information about the RV.

The gold standard for assessing RV function and RV–pulmonary artery (PA) coupling is construction of multi-beat pressure–volume

This is an open access article under the terms of the Creative Commons Attribution-NonCommercial License, which permits use, distribution and reproduction in any medium, provided the original work is properly cited and is not used for commercial purposes.

© 2025 The Author(s). *Pulmonary Circulation* published by John Wiley & Sons Ltd on behalf of Pulmonary Vascular Research Institute.

loops (PV loops) that measure pressure and volume changes throughout the cardiac cycle in response to varying loads [10–12]. Multi-beat PV loops measure the end-systolic elastance (Ees), a load-independent measure of contractility, and effective arterial elastance (Ea), a lumped measure of total ventricular afterload [10, 13]. The ratio of elastances, Ees/Ea, is used as a coupling measure that describes the extent to which right ventricular contractile function adapts to RV afterload [10, 13]. Prior studies have established cut-points of Ees/Ea associated with clinical worsening (CW) in PH, and PV loop phenotypes based on visual assessment of loop shape are associated with distinct clinical features [10, 13]. However, constructing multi-beat PV loops is technically challenging, and few practitioners can make these measurements. Therefore, there is a need to map readily available hemodynamic and RV-centric measurements to PV loop phenotypes.

Conventional clinical measurements include right heart catheterization (RHC), with and without exercise, and in some centers, cardiac magnetic resonance imaging (CMR) [12, 14–16]. These methods generate measurements that quantitatively describe RV function. While RHC and CMR cannot directly measure RV–PA coupling, estimates of RV–PA coupling can be derived via the single-beat method [17, 18], and prior studies have shown that various RHC and CMR measurements are correlated with multi-beat RV–PA coupling [19–22]. While the ability of PV loop metrics to predict PH prognosis has been established [19, 20], the effect of integrating several PV loop metrics using unsupervised machine learning to derive distinct RV–PA functional phenotypes has not been explored. Moreover, advanced machine learning methods that can integrate and prioritize multiple conventional clinical measurements (using a combination of linear and nonlinear methods) to predict PV-loop derived RV phenotypes have not been leveraged.

In this study, we sought to derive distinct patient risk groups via unsupervised clustering on PV loop data alone. We hypothesized that modeling clinically accessible hemodynamic and RV functional measures would allow for accurate prediction of the derived PV loop clusters. Here, we characterize three patient groups with distinct PV loop phenotypes. We present a random forest classifier that integrates conventional RV-centric measurements to predict these patient PV loop groups (AUC = 0.93). Finally, we probe this classifier to identify which conventional measurements are most predictive of RV phenotype.

2 | Methods

2.1 | Study Subjects

One hundred and one subjects were prospectively recruited into a continuously enrolling PV loop cohort at our center (Table 1). Subjects were referred to the study team by treating clinicians recommending a clinical RHC for known or suspected PH. All enrolled subjects granted informed consent to a protocol for an extended catheterization that included exercise and PV loop measurements that is approved by the Institutional Review Board of Johns Hopkins Medicine. In addition to RHC, subjects underwent same-day CMR according to a previously published protocol for volume calibration [20]. After hemodynamic and imaging data were collected, subjects were followed prospectively for ascertainment of outcomes, including time to clinical worsening (CW), defined as the time period between catheterization and the first occurrence of one of the following events: death, transplant, hospitalization for right heart failure, worsening of New York Heart Association functional class (NYHA FC), decline in 6-min walk test (6MWT), and escalation of PAH-specific therapy. PH groups were classified according to the hemodynamic and clinical definitions set forth in the 2022 European Society of Cardiology/European Respiratory Society Guidelines [23].

2.2 | PV Loop Measurements

After the standard RHC procedure, a dual-entry 9F sheath (#406333, St. Jude's Medical, St. Paul, MN) was used to facilitate the simultaneous placement of a 5F PV catheter (SPC-570-2, Millar Instruments, Houston, TX), and a 4F balloon-tipped PA wedge catheter (AI-07122, Teleflex, Morrisville, NC). Under fluoroscopic guidance, the PV catheter was carefully advanced until the pigtail tip reached the RV apex. The resulting signals generated from individual electrode pairs on the catheter were examined and summed to produce the total volume, with only those signals that were in phase and consistent with an intracavitary position being used. Steady-state data were measured during a Valsalva maneuver and at end-expiration, using a multi-beat decline in RV end-diastolic filling, as previously described and validated [10]. To create a family of pressure–volume loops, preload was reduced using a Valsalva maneuver and manual external inferior vena cava compression if necessary. This method has been previously validated [10]. Real-time data acquisition was reviewed by two experienced investigators to ensure that preload reduction was adequate to enable determination of the end-systolic pressure–volume relationship. Multiple loops from both steady state and preload measurements were averaged for analysis.

After collecting baseline PV data, subjects were positioned onto a supine bicycle ergometer. The subjects then underwent bicycle exercise using a modified protocol, with the starting stage set at 15 W and 10-W increments every 2-min stage until the maximum effort that was symptom-limited was achieved. Throughout the exercise, PA pressures, gas exchange, and PV data were continuously recorded.

2.3 | Identification of Unique PV Loop Patient Groups

Before analyzing PV loop measurements, we filtered our data set to obtain one with no missing values. Our initial data set contains 101 patients with 19 PV loop measurements (EDP, EDV, ESV, SV, Ees, Ea, Ees/Ea, V0, PRSW, SW, *dp*/*dt*-max, *dp*/*dt*-min, *dp*/*dt*-IP, PWR-max, PWR-max/EDV, Peak Flow Rate/EDV, Tau-Glantz, Tau-Weiss, and Tau-Suga). To handle missingness, we first removed features that contained missing values for > 60% of patients. This process led to the removal of nine features. Then, we removed patients who were missing values for the maintained 10 features. After data filtering, the data set consisted of 64 patients and 10 PV loop features (EDV, ESV, Ees, Ea, Ees/Ea, V0, PRSW, SW, *dp*/*dt*-

20458940, 2025, 1, Downloaded from https://onlinelibrary.wiley.com/doi/10.1002/pul2.70057, Wiley Online Library on [11/12/2025]. See the Terms and Conditions (https://onlinelibrary.wiley.com/terms-and-conditions) on Wiley Online Library for rules of use; OA articles are governed by the applicable Creative Commons License

TABLE 1 | Demographics and clinical characteristics for PV loop patient groups.

	Overall ($n = 64$)	Best ($n = 26$)	Median ($n = 23$)	Worst ($n = 15$)
Demographics				
Sex (female/male) (% n)	88/13	92/8	78/22	93/7
Race (White/Black/Hispanic/Asian) (n)	48/9/3/2	22/1/2/0	14/6/1/2	12/2/0/0
Clinical characteristics				
Functional Class (1, 2, 3) (n)	7/36/21	4/16/6	2/14/7	1/6/8
WSPH Group (I, II, III, IV, V) (n)	37/4/8/0/0	9/3/4/0/0	13/1/4	15/0/0/0/0
Age (median ± IQR)	58.0 ± 19.5	64.0 ± 12.8	48.0 ± 16.5	56.0 ± 22.5
Height (m, median ± IQR)	1.6 ± 0.1	1.6 ± 0.1	1.6 ± 0.1	1.6 ± 0.1
Weight (kg, median ± IQR)	75.0 ± 26.9	66.4 ± 19.0	82.6 ± 25.3	73.9 ± 34.9
BMI (mean ± SD)	28.7 ± 6.2	27.2 ± 5.4	29.6 ± 5.9	29.7 ± 7.6
Pro-BNP (pg/mL, median ± IQR)	422.3 ± 568.2	285.7 ± 283.5	311.6 ± 398.2	819.9 ± 905.7
Creatinine (mg/dL, median ± IQR)	0.8 ± 0.2	0.8 ± 0.4	0.8 ± 0.2	0.9 ± 0.3
6 min walk distance (meters, median ± IQR)	402.8 ± 116.7	394.8 ± 90.6	431.4 ± 120.4	372.4 ± 147.6
RAP (mmHg, median ± IQR)	5.0 ± 5.0	4.0 ± 4.8	5.0 ± 3.5	7.0 ± 6.5
mPAP (mmHg, median ± IQR)	27.0 ± 17.0	24.5 ± 8.8	27.0 ± 8.5	50.0 ± 13.0
PCWP mean (mmHg, median ± IQR)	9.5 ± 5.2	9.5 ± 6.0	9.0 ± 4.5	10.0 ± 5.0
TDCO (L/min, median ± IQR)	4.6 ± 1.5	4.6 ± 1.1	5.1 ± 1.8	4.2 ± 1.8
TDCI (L/min/m^2, mean ± SD)	2.6 ± 0.6	2.7 ± 0.5	2.6 ± 0.7	2.3 ± 0.6
PA saturation (%, mean ± SD)	68.9 ± 4.5	69.1 ± 4.2	69.8 ± 4.9	66.9 ± 4.2
PVR from TDCO (WU, median ± IQR)	4.1 ± 4.0	2.7 ± 2.3	3.3 ± 3.7	9.5 ± 5.5
Treatment characteristics at the time of catheterization				
Monotherapy (%)	12.5	3.8	21.7	13.3
Dual therapy (%)	23.4	19.2	26.1	26.7
Triple therapy (%)	1.6	0.0	0.0	6.7

max, dp/dt-min) with no missing values. Excluded patients have similar demographic features to those included for this analysis (Supporting Information S1: Table 1). Then we performed z-score scaling on the data, such that each feature had a mean of zero and standard deviation of one. We performed unsupervised k-means clustering on the PV loop data set described above. We quantified the inertia, or within-group standard deviation, for increasing values of k, and identified the optimal k value as the threshold after which inertia drop-off is no longer significant (i.e., elbow method).

2.4 | Quantification of COMPERA and REVEAL Lite 2.0 Risk Scores

For each subject, we calculated the COMPERA and REVEAL Lite 2.0 risk scores to generate a clinically relevant classification scheme for comparison with PV loop clusters. The COMPERA risk score utilizes NYHA FC, 6MWT, and pro-brain natriuretic peptide (pro-BNP) level to assign a risk score of 1–4, where 1 indicates low risk, 2 intermediate-low risk, and 3 indicates high risk [9]. The REVEAL Lite 2.0 risk score approximates the REVEAL risk score with fewer metrics; this risk score utilizes NYHA FC, 6MWT, and pro-brain natriuretic peptide (pro-BNP), systolic blood pressure, heart rate, and estimated glomerular filtration rate to ascribe low, intermediate, or high risk [7, 8].

2.5 | Assessment of CW and Statistical Testing

We generated Kaplan Meier curves of time to CW for the PV loop-derived patient groups. CW was defined as the occurrence of any of the following events: death, transplant, hospitalization for RV failure, worsening of NYHA FC, decline in 6MWT (> 15%), and escalation of PAH-specific therapy (beyond upfront treatment prescribed at the time of diagnosis). Time to CW was measured as the time between the date of catheterization to the date of the earliest recorded worsening event [10]. We also phenotyped the PV-loop clusters by statistically comparing values for PV loop variables and standard clinically available measurements between the three clusters. For normally distributed variables, we conducted an ANOVA test followed by a Tukey's t-test for post hoc testing. For variables that were not normally distributed, we conducted a Kruskal–Wallis test followed by the Dunn test for post hoc comparisons.

2.6 | Predictive Classifier Training and Model Selection Criteria

To assess the predictability of the three unique PV loop patient groups, we trained and evaluated classification models on different sets of clinically obtainable features (RHC rest, RHC exercise, CMR)

20458940, 2025, 1, Downloaded from https://onlinelibrary.wiley.com/doi/10.1002/pul2.70057, Wiley Online Library on [11/12/2025]. See the Terms and Conditions (https://onlinelibrary.wiley.com/terms-and-conditions) on Wiley Online Library for rules of use; OA articles are governed by the applicable Creative Commons License

and a combined set of all clinical features (All Features). For each feature set we applied the data filtration and scaling strategy outlined in the Identification of unique PV loop patient groups section. In addition to the data filtration process above, we ran a Spearman cross-correlation analysis to determine highly correlated features and eliminated features such that all features have a correlation coefficient < 0.95. We decided to not exclude any exercise hemodynamic features as an exception, because these features were already very sparse in our data set. The final features used in each feature set are listed in Table 2. For each feature set, the data were randomly split into two groups comprised of a training data set (60% of the patients) and a holdout testing data set (40% of the patients) for unbiased testing.

2.6.1 | Model Training and Hyperparameter Tuning

We trained Multinomial Logistic Regression [24], Random Forest [25], and Extreme Gradient Boost [26] models. Logistic regression models exploit generalized linear models to derive a decision boundary between outcomes, while random forest and XGBoost models learn a tree-based decision structure to classify samples. Each model has several respective hyperparameters that determine optimization rate, regularization strength, bootstrapping, and tree structure. To choose the optimal set of hyperparameters that maximize the model prediction accuracy, we performed hyperparameter tuning using a grid search algorithm on each model for each feature set. We used sevenfold cross-validation to prevent overfitting and improve robustness during model training. We selected the model that maximized the mean cross-validation training accuracy, micro-averaged area under the receiver operating curve, and micro-averaged $F1$ score [27, 28]. We tested this model on held-out data.

2.6.2 | SHAP Analysis of Selected Model

We estimated the impact of each feature on the output predictions of the selected model by performing a SHAP (Shapley additive explanations) analysis [29] on model ability to perform predictions on the held-out data. The absolute SHAP value quantifies how much a singular feature affected the prediction, which is the PV loop patient group. Features with the greatest SHAP values are the top predictive features.

2.7 | Statistical Package

All statistical computations were conducted in Python using the SciKit-Learn library.

3 | Results

3.1 | Cohort Demographics

Our patients were, on average, in the sixth decade of life and predominantly female (87.5%) and white (75%). Subjects had mild/moderate PH, with mean pulmonary arterial pressure (mPAP) of 31.5 ± 13.8 mmHg, PVR 5.13 ± 4.14 Woods Units, and WHO functional Class 2 (56%) or 3 (32%) symptoms. Patients primarily had WSPH Group 1 disease (Table 1).

3.2 | Derivation of Clinically Distinct Patient Groups Based on PV Loop Data

To derive distinct emergent PV loop phenotypes, we applied unsupervised k-means clustering to a cohort of 64 patients (Figure 1) with the following PV loop measurements: baseline RV volume ($V0$, mL), right ventricle end diastolic right volume (RVEDV, mL), right ventricle end systolic volume (RVESV, mL), right ventricle end systolic elastance (Ees, mmHg/mL), pulmonary arterial elastance (Ea, mmHg/mL), coupling (Ees/Ea), preload recruitable stroke work (PRSW, mmHg), stroke work (SW, mmHg), maximum derivative of pressure (dp/dt-max, mmHg/min), and minimum derivative of pressure (dp/dt-min, mmHg/min).

Patients clustered into three groups in the dimensionally reduced space (Figure 1A). Patient groups exhibited a trend toward different times to CW (log-rank $p = 0.096$, p for trend $= 0.034$) (Figure 1B). We labeled the three patient groups as "best," "median," and "worst" based on time to CW, PV-loop features, and standard clinically available measurements. Because this data set includes a mix of Group 1 and non-Group 1 PH patients, we repeated testing of PV loop phenotype prediction of time to CW in only Group 1 patients, and found a similar trend (log-rank $p = 0.096$, p for trend $= 0.034$). Notably, all patients who experienced events in the all-PH analysis were Group 1 patients.

Patients within each risk group demonstrated distinct RV–PA phenotypes (Figure 1C, Table 3 and Supporting Information: Tables 2 and 3). RV volumes, indicative of dilation of the RV, were highest in the "median" patient group, and CMR RVEF was also lowest in the "median" group. The "worst" patient group demonstrated the lowest Ees/Ea ratio, consistent with prior data associating RV–PA uncoupling with worse clinical outcomes [10], while Ees/Ea was > 1 in both "best" and "median" groups. A similar proportion of patients across all groups demonstrated contractile reserve, defined as a positive change in Ees during exercise. The "worst" group demonstrated steep increases in mPAP with exercise and a blunted change in CO. The "median" and "worst" groups demonstrated higher values for stroke work and a larger range between minimum and maximum pressure derivatives.

To visualize how PV loop-derived risk groups align with the current PH risk stratification schema, we generated Sankey plots to visualize reclassification of individuals across risk groups when applying PV loop phenotyping versus COMPERA (Figure 1D) or REVEAL Lite 2.0 (Figure 1E) risk scores for risk stratification. Indeed, each COMPERA and REVEAL Lite 2.0 risk score category contains several PV loop risk groups, suggesting that these PV loop groups capture physiologic information that may augment routine clinical risk stratification.

3.3 | Development of a Machine Learning Model to Predict PV Loop Group Using Standard Clinically Available Measurements

Because PV loop measurement is not a widely accessible technology, we hypothesized that we could integrate standard clinically available measurements to predict PV loop-derived patient groups. We tested three different models (multinomial logistic regression, random forest, and extreme gradient boost)

20458940, 2025, 1, Downloaded from https://onlinelibrary.wiley.com/doi/10.1002/pul2.70057, Wiley Online Library on [11/12/2025]. See the Terms and Conditions (https://onlinelibrary.wiley.com/terms-and-conditions) on Wiley Online Library for rules of use; OA articles are governed by the applicable Creative Commons License

TABLE 2 | Standard clinically available filtered features used to train the classifier model that predicts the PV loop patient group.

RHC rest	RHC exercise	CMR	All
• Systolic blood pressure (SBP, mmHg) • Diastolic blood pressure (DBP, mmHg) • Mean arterial pressure (MAP, mmHg) • Right atrial pressure (RAP, mmHg) • Right ventricle diastolic pressure (RVDP, mmHg) • Pulmonary artery systolic pressure (PASP, mmHg) • Mean pulmonary arterial pressure (mean PAP, mmHg) • Pulmonary capillary wedge pressure mean (PCWP mean, mmHg) • Thermodilution cardiac output (TDCO, L/min) • Thermodilution Cardiac Index (TDCI, L/min/m^2) • Pulmonary artery oxygen saturation (PA saturation, %) • Pulmonary vascular resistance from TDCO (PVR, WU)	• Mean pulmonary arterial pressure (leg raise) (mean PAP (leg raise), mmHg) • Pulmonary capillary wedge pressure (leg raise) (PCWP (leg raise), mmHg) • Mean pulmonary pressure (25 W) (mean PAP (25 W), mmHg) • Mean pulmonary pressure (Peak) (mean PAP (Peak), mmHg) • Peak workload (watts)	• Left ventricle end-diastolic volume (LV ED vol, mL) • Left ventricle end-diastolic body surface area (LV ED BSA, m^2) • Left ventricle end-systolic volume (LV ES Vol, mL) • Left ventricle stroke volume (LV SV, mL) • Left ventricle cardiac output (CMR) (LV CO (CMR), L/min) • Left ventricle ejection fraction (LVEF, %) • Left ventricle end diastolic mass (LVED mass, g) • Right ventricle end diastolic volume (RV ED vol, mL) • Right ventricle end systolic volume (RV ES vol, mL) • Right ventricle end diastolic mass (RVED mass, g) • Right ventricle ejection fraction (RVEF, %)	All previously selected for filtered features

on four different feature sets (RHC rest, RHC exercise, CMR, and the combination of all three). We assessed model performance using training accuracy, area under the curve (AUC), and $F1$ scores (Table 4). The highest performing model was a random forest classifier trained on all measurements (mean cross-validation accuracy = 0.76 and maximal training area under the curve and training $F1$ score).

Based on our selection criteria of maximizing training accuracy, area under the curve, and $F1$ score, we selected the highest-performing random forest model to test on held-out data. Our random forest model yielded a testing micro-average AUC of 0.93 (Figure 2A) and testing micro-average $F1$ score of 0.73 (Figure 2B). Because our model was trained on a small sample ($n \sim 30$), we used Monte-Carlo simulations to test for overfitting (Figure 2C). We randomly shuffled the labels on our data set and used our trained model to predict outcomes. Our simulations yielded an average accuracy of 0.35, which is close to the expected value of 0.33 for a prediction problem with three outcomes. Moreover, none of the simulations yield an accuracy greater than or equal to our testing accuracy, providing confidence that the model is not overfit.

To assess which standard clinically available measurements critically impacted model predictions, we performed a SHAP analysis on our random forest model (Figure 3). Our SHAP analysis indicates mPAP at 25 W exercise, mPAP at rest, CMR-derived right ventricular end systolic volume, right ventricular ejection fraction, and left ventricular end systolic volume as the top five predictive features. Thus, the model selected a combination of RHC and CMR features to predict PV loop phenotype.

3.4 | RHC and CMR Measurements Distinguishing PV Loop Phenotypes Predict Time to Clinical Worsening

Because our PV loop phenotypes exhibited different time to clinical worsening trends, we tested whether the top predictive features from our RF classifier predicted time to clinical worsening. To test this hypothesis, we constructed individual Cox proportional hazard models for the top four predictive features identified by SHAP analysis. Each predictor variable was indeed significantly associated with time to clinical worsening ($p \leq 0.05$ for each, Supporting Information S1: Table 4). Thus, our overall

20458940, 2025, 1, Downloaded from https://onlinelibrary.wiley.com/doi/10.1002/pul2.70057, Wiley Online Library on [11/12/2025]. See the Terms and Conditions (https://onlinelibrary.wiley.com/terms-and-conditions) on Wiley Online Library for rules of use; OA articles are governed by the applicable Creative Commons License

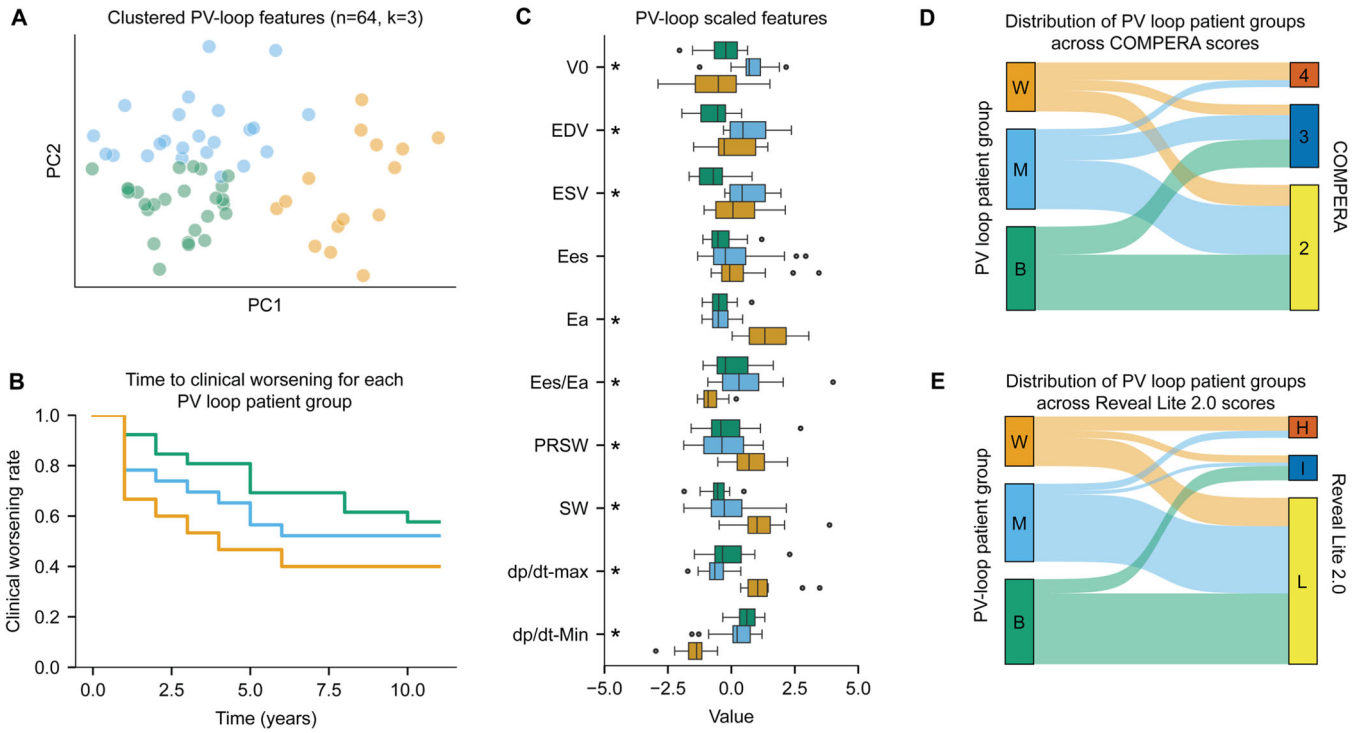

FIGURE 1 | Identification of three patient groups with varying clinical outcomes using PV loop features. (A) PCA dimensionality reduction of patients colored by labels found using unsupervised *k*-means clustering. (B) Time to clinical worsening curves for each PV loop patient group. (C) *Z*-score scaled distributions of PV loop parameters in each PV loop patient group. * indicates p value < 0.05 for multi-group statistical testing (either one-way ANOVA or Kruskal–Wallis). (D) Sankey plot for $n = 61$ patients, describing how COMPERA risk scores map to emergent PV loop patient groups. (E) Sankey plot for $n = 60$ patients, describing how Reveal Lite 2.0 risk scores map to emergent PV loop patient groups. "L" indicates low risk, "I" indicates intermediate risk, and "H" indicates high risk.

TABLE 3 | PV loop features for Best, Median, and Worse groups identified using *k*-means clustering.

	Best	Median	Worse	*p*	*p (B vs. M)*	*p (B vs. W)*	*p (M vs. W)*
EDV (mL)	119.7 ± 22.9	173.0 ± 33.2	149.3 ± 36.2	< 0.001	0.001	0.010	0.055
ESV (mL)	53.7 ± 18.4	95.9 ± 23.8	84.7 ± 33.9	< 0.001	0.001	0.001	0.365
Ees (mmHg/mL)	0.6 ± 0.2	0.8 ± 0.4	0.9 ± 0.5	0.075			
Ea (mmHg/mL)	0.5 ± 0.2	0.5 ± 0.2	1.4 ± 0.4	< 0.001	0.912	< 0.001	< 0.001
Ees/Ea	1.2 ± 0.6	1.6 ± 0.9	0.7 ± 0.3	< 0.001	0.215	0.002	< 0.001
V0 (mL)	−9.7 ± 28.8	35.5± 28.4	−24.5 ± 52.1	< 0.001	0.001	0.411	0.001
PRSW (mmHg)	20.2 ± 7.4	19.2± 8.2	28.2 ± 6.6	0.001	0.866	0.005	0.002
dp/dt-max (mmHg/min)	425.1 ± 111.8	370.8 ± 67.4	615.5 ± 118.4	< 0.001	0.118	< 0.001	< 0.001
SW (mmHg)	1790.6 ± 579.4	2276.3 ± 1122.2	4019.4 ± 1296.2	< 0.001	0.160	< 0.001	< 0.001
dp/dt-min (mmHg/min)	−3478.0 ± 83.6	-413.2 ± 141.5	−733.5 ± 121.1	< 0.001	0.157	< 0.001	< 0.001
Contractility reserve (% yes/% no)	52%/48%	47%/53%	50%/50%				
Contractility reserve (mmHg/mL)	0.06 ± 0.21	0.05 ± 0.28	0.32 ± 0.95	0.99			

Note: For each feature, we report the average ± SD. The reported p value indicates results for an ANOVA with post hoc Tukey tests or Kruskal–Wallis test with post hoc Dunn test based on whether the variable is normally distributed. Gray boxes indicate features for which post hoc testing was not conducted because multiple group testing did not yield a $p < 0.05$. Contractility reserve was computed as the difference between Ees during 25 W exercise and at baseline for patients with available data ($n = 54$).

20458940, 2025, 1, Downloaded from https://onlinelibrary.wiley.com/doi/10.1002/pul2.70057, Wiley Online Library on [11/12/2025]. See the Terms and Conditions (https://onlinelibrary.wiley.com/terms-and-conditions) on Wiley Online Library for rules of use; OA articles are governed by the applicable Creative Commons License

approach identified accessible RV-centric measurements predictive of both PV loop phenotype and time to clinical worsening.

4 | Discussion

Here, we demonstrate that with quantitative multi-parameter assessment of PV loop data, distinct RV functional phenotypes emerge. Because PV loop analysis is infrequently performed in the clinical setting, we identified conventional RHC and CMR measurements which could accurately predict these phenotypes with high discrimination (AUC 0.93). This work provides proof of principle that combinations of clinically accessible hemodynamic and imaging measurements can predict unique RV phenotypes that can only be derived using complex research methods. Because our ability to understand RV function using the individual clinical tools currently at our disposal is limited, leveraging aggregated data in this way could allow for a more nuanced understanding of RV function.

Prior studies have demonstrated that reduced RV–PA coupling, as measured by multi-beat Ees/Ea, is associated with worse clinical outcomes [6, 10–12]. Given the relevance of Ees/Ea in representing RV adaptation and predicting PH prognosis, investigators have attempted to characterize coupled versus uncoupled RV–PA units using more accessible measurements [19, 21, 22]. For example, one study identified Ees/Ea < 0.68 as a predictor of reduced survival, then stratified RV functional metrics according to this cutoff, finding higher RV volumes, higher RV mass, and lower RVEF in subjects with Ees/Ea < 0.68, and concluding that adaptive coupling was associated with preserved RV size and function [19]. Generally, RV dilation is regarded as a mechanism of heterometric adaptation, whereby ventricular dilation serves to increase stroke volume and cardiac output after contractility cannot be further augmented to match load [30]. The results of our unbiased multi-parameter assessment, however, suggest a more nuanced picture, demonstrating a distinct group of patients in our cohort with RV dilation and dysfunction, yet preserved coupling.

Measurement of PV loops generates rich data that allows for calculation of metrics beyond Ees/Ea, including PRSW, SW, *dp*/*dt*-maximum, and *dp*/*dt* minimum. The elucidation of distinct phenotypic groups accomplished by integrating these metrics suggests that the RV's ability to adapt to load may be best gauged by multi-parameter assessment. For example, Ees/Ea did not differ significantly between the "best" and "median" phenotypes. Moreover, the phenotypic group with highest RV volumes and lowest RVEF (features typically accessible to and weighed by clinicians) did not demonstrate the worst survival. The "worst," highest-risk RV phenotype in our cohort demonstrated intermediate increases in RV volumes, high Ea, and low Ees/Ea. Our results are limited to phenotypic descriptions and do not shed light on reasons for the unexpected relationships between energetic coupling, RV dilation, and systolic function. The possible factors underlying these discrepancies are worthy of future directions in research, including potential differences in intrinsic myocardial properties, metabolic adaptation and substrate utilization, wall stress, septal mechanics, and ventricular interdependence. Taken together, however, our phenotypic descriptions suggest assessment of a single RV feature in isolation may be misleading, and aggregating data may improve assessment.

Several previous studies have demonstrated ratios of individual echo or CMR measurements might serve as noninvasive surrogates for coupling [19–22]. The best validated among these is the echocardiographic tricuspid annular plane systolic excursion to estimated pulmonary arterial systolic pressure (TAPSE/PASP) ratio [31]. However, individual predictors such as TAPSE/PASP have generally shown good discrimination of coupled from uncoupled RV–PA units as a dichotomous outcome, while continuous correlations with Ees/Ea have been more modest. Our work demonstrates that an alternative to this approach is made feasible by leveraging advanced data driven techniques. Here, we show that classifiers can be trained that integrate several accessible RV-centric measurements to predict more granularly defined patient groups displaying unique phenotypes (as opposed to a coupled vs. uncoupled dichotomy) that might convey higher-level information about RV function. If validated in larger sample sets, such an approach may provide a more precise means of personalizing RV functional assessment.

A few studies have taken differing approaches to multi-parametric assessment of RV phenotypes. Assignment of phenotype based on visual assessment of multi-beat PV loop shape (triangular, quadratic, trapezoid, or notched) has been associated with disease severity in patients with PAH [6]. Trapezoid and notched shapes were associated with higher mPAP, higher stroke work, impaired PA compliance, and lower Ees/Ea. Recently, Janowski et al. reported the results of consensus clustering of variables derived from RV pressure waveforms obtained at their center using the single beat method [32]. They generated five distinct clusters differentiated by coupling, contractility, and diastolic stiffness. Their input variables and cluster phenotypes differed from ours, but they also uncovered unique patterns (e.g., one phenotype was characterized by RV dilation with RVEF but reduced Ees/Ea) and also found that assignment to one particular cluster (Cluster 4) was predictive of survival. In contrast to our study, Janowski et al. did not consider exercise hemodynamics in clustering, and they did not generate multi-beat loops.

In our cohort, the low number of mortality events captured during time under observation was insufficient for us to examine PV loop phenotype associations with survival, and we were only able to examine associations with time to clinical worsening. This limits the interpretability of comparisons of our phenotypes with current clinical risk scores. However, our analysis allows visualization of the reclassification of individuals across risk groups when applying PV loop phenotyping versus clinical risk scores (Figure 1D,E). The plots show that risk assessment varies substantially depending on the score applied. Each PV loop risk group consists of patients from several different COMPERA and REVEAL risk strata, suggesting that by capturing unique ventriculo-arterial parameters, these PV loop risk groups may have potential to augment the noninvasive risk stratification schemes typically applied clinically. To date, RV function has not been well-integrated into PH risk assessment, despite studies showing improved prognostication by supplementing traditional risk calculators with RV imaging metrics [33, 34]. Our study results support these prior findings by showing that PV loop

20458940, 2025, 1, Downloaded from https://onlinelibrary.wiley.com/doi/10.1002/pul2.70057, Wiley Online Library on [11/12/2025]. See the Terms and Conditions (https://onlinelibrary.wiley.com/terms-and-conditions) on Wiley Online Library for rules of use; OA articles are governed by the applicable Creative Commons License

TABLE 4 | Classifier scoring metrics on training data for distinct feature sets.

	RHC rest	RHC exercise	CMR	All
Train dimensions ($n \times$ d)	(39, 12)	(34, 5)	(38, 11)	(33, 28)
Test dimensions ($n \times$ d)	(27, 12)	(23, 5)	(26, 11)	(22, 28)
Logistic regression				
Mean cross-validation accuracy	0.638	0.707	0.714	0.729
Training *F*1 micro-average	0.667	0.706	0.816	0.848
Training AUC micro-average	0.871	0.872	0.918	0.943
Random Forest Classifier				
Mean cross-validation accuracy	0.619	0.650	0.781	**0.757**
Training F1 micro-average	0.974	0.794	0.974	**1.0**
Training AUC micro-average	1.000	0.956	0.999	**1.0**
Extreme gradient boost (XGBoost)				
Mean cross-validation accuracy	0.662	0.529	0.729	0.657
Training F1 micro-average	0.769	0.676	0.921	0.879
Training AUC micro-average	0.945	0.860	0.991	0.988

Note: The highest performing model was selected based on having consistently high values across mean cross-validation training accuracy, micro-averaged training AUC, and micro-averaged training *F*1 score.

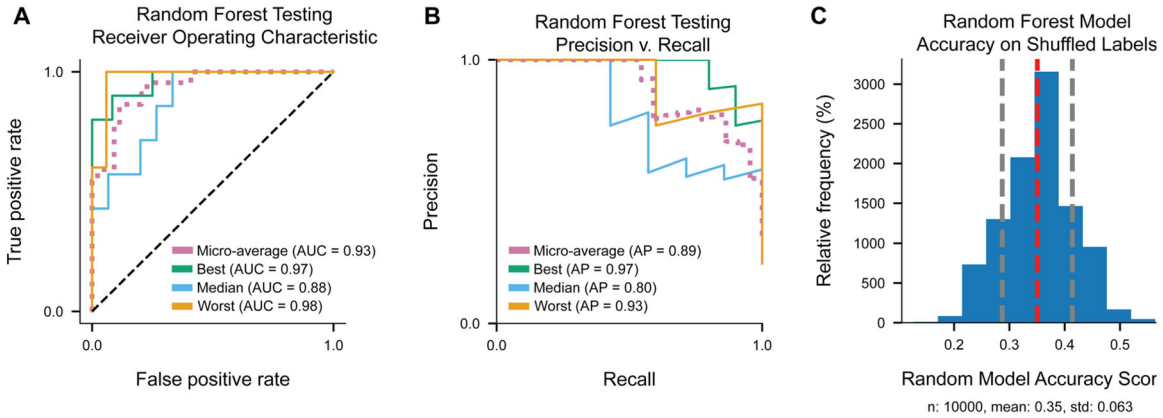

FIGURE 2 | Random forest model performance on predicting PV loop patient group. (A) Receiver-operating characteristic curve and (B) the precision–recall curve for the random forest model indicate high predictive power when integrating all four data subsets. "AP" indicates average precision. (C) Testing trained random forest model on data with randomly shuffled labels indicates an accuracy of ~35%.

phenotypes do not neatly map onto current risk stratification schemes, suggesting additional information is gained by considering ventriculoarterial parameters.

Analyzing feature importance in our random forest classifier identifies the top clinical predictors of PV loop phenotype. SHAP analysis indicates mPAP at 25 W exercise, mPAP at rest, right ventricular end systolic volume, right ventricular ejection fraction, and left ventricular end systolic volume were the top five predictive features of PV loop phenotypes in our cohort. These features align with prior studies that have attempted to map individual RV-centric measurements to PV loop variables [16, 19]. Our finding that one of the most predictive features was exercise mPAP underscores the potential utility of exercise hemodynamics, which have been associated with PH prognosis in recent studies [3, 35–37]. While exercise hemodynamics have traditionally been investigated for utility in unmasking occult pulmonary vascular disease in patients with normal resting hemodynamics, our result suggests they may also be informative for understanding RV function and RV–PA interactions in patients with known PH. Our data do not fully explain why this could be, though we suspect in known PH patients with poor pulmonary vascular recruitability and distensibility, steep mPAP increases with exercise, coupled with an inability of the RV to augment CO during exercise (as seen in our "worst" group), may indicate poor RV reserve. Consistent with this possibility, we have recently shown that poor CO reserve is associated with RV stiffness and higher exercise afterload [38]. It is also possible that RV function mediates the relationship between resting mPAP and exercise mPAP in PH patients with poor vascular compliance, and thus these variables together report on RV health. Notably, exercise-induced PH was re-introduced as a recognized disease entity in the latest 2022 ESC/ERS Guidelines for the diagnosis and treatment of PH based on the clinical utility of exercise hemodynamics for detecting occult pulmonary vascular disease and predicting progression to

20458940, 2025, 1, Downloaded from https://onlinelibrary.wiley.com/doi/10.1002/pul2.70057, Wiley Online Library on [11/12/2025]. See the Terms and Conditions (https://onlinelibrary.wiley.com/terms-and-conditions) on Wiley Online Library for rules of use; OA articles are governed by the applicable Creative Commons License

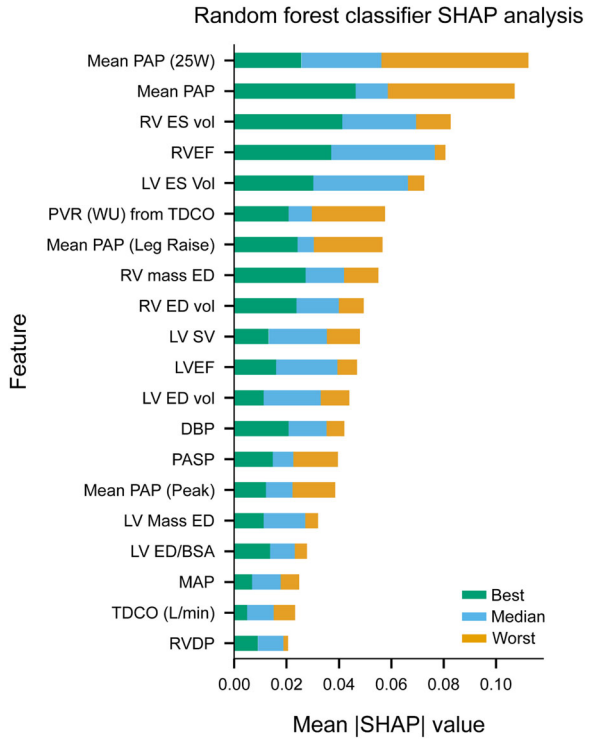

FIGURE 3 | SHAP analysis of the random forest model indicates top predictive features of the PV loop patient group.

overt resting PH [23]. While exercise hemodynamics are currently most commonly obtained in specialized centers, it may be worth advocating for broader adoption of exercise RHC moving forward.

There are several limitations to the present study. The cohort consisted of 64 patients after data filtration, and this modest sample size could both skew predictions and penalize establishment of statistical significance. Further, data were complete for only 10 of the 19 original PV loop variables. Because PV loop construction is both expensive and only possible in a few centers, low cohort size and missing data are common limitations of work involving these measurements. We chose to defer multiple imputation strategies in favor of a complete-case analysis, but it is possible we filtered out variables that would further refine RV functional phenotypes. To maximize statistical power for our analyses, we chose to study a combination of Group 1 and Non-Group 1 PH patients, which could limit the generalizability of results to certain PH subgroups, including Group 1 patients. On the other hand, our unbiased derivation of emergent PV phenotypes in the data set was agnostic of current approaches to clinical classification, and, the 10 PV loop features we analyzed yielded distinct and relevant phenotypes. One practical limitation of our work is that the top-most predictive feature was exercise mPAP, which, as discussed above, may not be available in some centers. Future studies should build upon this work by integrating higher-dimensional RV-centric data to refine more granular phenotypes and identify sparse sets of predictors, perhaps within clinically recognized PH subgroups, and improve the accuracy of predictive models.

In conclusion, here we apply data-driven modeling to identify three PV loop-derived RV phenotypes that can be readily discriminated by more accessible clinical parameters. This work demonstrates that clinically accessible hemodynamic and non-invasive imaging measurements can predict unique RV functional phenotypes with high fidelity. Because our ability to understand patient-level RV function is currently somewhat limited, this demonstrated ability to infer granular phenotypic information typically only available via PV loop measurement could allow for a more nuanced view of RV function in the clinical arena. As additional patients enroll into our cohort and our sample size increases, we can consider re-analyzing the data with imputation strategies that allow inclusion of features that might refine our phenotypes. As additional events accrue in the cohort, we can formally test the impact of RV-based phenotypes on mortality risk prediction. Future avenues of investigation that leverage similar data-driven approaches to analyzing research-based feature sets could yield clinically meaningful improvements to current risk stratification schemes. Further study is needed to determine how best to incorporate RV-centric metrics into clinical risk prediction.

Author Contributions

Nikita Sivakumar and Catherine E. Simpson designed the study. Nikita Sivakumar, Catherine E. Simpson, Cindy Zhang, Connie Chang-Chien, Pan Gu, Yikun Li, and Yi Yang performed statistical analysis and interpreted quantitative results. Darin Rosen, Tijana Tuhy, Ilton M. Cubero Salazar, Matthew Kauffman, Rachel L. Damico, Steven Hsu, and Paul M. Hassoun acquired, maintained, and interpreted clinical data and contextualized results. Joseph L. Greenstein and Casey Overby Taylor provided critical input into designing and interpreting computational analyses. Nikita Sivakumar, Cindy Zhang, and Catherine E. Simpson drafted the manuscript, and all authors contributed revisions. All authors approved the final, submitted draft of the manuscript.

Acknowledgments

The authors wish to acknowledge Karen Yang and Ilia Rattsev for assistance with using computational resources for the completion of this work. C.E.S. had complete access to the data and takes full responsibility for the conduct of the work and overall content of the manuscript. This work was supported by NIH 1L30HL165545-01 (to I.M.C.S.), NIH 5T32HL007227-47 (to I.M.C.S), NIH/NHLBI K23HL153781 (to C.E.S.), R01HL114910 (to P.M.H.), and K23HL146889 (to S.H.).

Ethics statement

All human subjects provided informed consent before enrollment in a research protocol approved by the Institutional Review Board of The Johns Hopkins University School of Medicine.

Conflicts of Interest

Paul M. Hassoun serves on a scientific steering board for MSD, an activity unrelated to the current work. Rachel L. Damico has received payments for expert witness testimony regarding unrelated matters. The other authors declare no conflicts of interest.

References

1. J. R. Sysol and R. F. Machado, "Classification and Pathophysiology of Pulmonary Hypertension," *Continuing Cardiology Education* 4 (2018): 2–12.

2. A. Vonk Noordegraaf, K. M. Chin, F. Haddad, et al., "Pathophysiology of the Right Ventricle and of the Pulmonary Circulation in Pulmonary Hypertension: An Update," *European Respiratory Journal* 53 (2019): 1801900.

20458940, 2025, 1, Downloaded from https://onlinelibrary.wiley.com/doi/10.1002/pul2.70057, Wiley Online Library on [11/12/2025]. See the Terms and Conditions (https://onlinelibrary.wiley.com/terms-and-conditions) on Wiley Online Library for rules of use; OA articles are governed by the applicable Creative Commons License

3. C. G. Ireland, R. L. Damico, T. M. Kolb, et al., "Exercise Right Ventricular Ejection Fraction Predicts Right Ventricular Contractile Reserve," *Journal of Heart and Lung Transplantation* 40 (2021): 504–512.

4. M. C. van de Veerdonk, T. Kind, J. T. Marcus, et al., "Progressive Right Ventricular Dysfunction in Patients With Pulmonary Arterial Hypertension Responding to Therapy," *Journal of the American College of Cardiology* 58 (2011): 2511–2519.

5. R. J. Tedford, J. O. Mudd, R. E. Girgis, et al., "Right Ventricular Dysfunction in Systemic Sclerosis-Associated Pulmonary Arterial Hypertension," *Circulation: Heart Failure* 6 (2013): 953–963.

6. M. J. Richter, S. Hsu, A. Yogeswaran, et al., "Right Ventricular Pressure-Volume Loop Shape and Systolic Pressure Change in Pulmonary Hypertension," *American Journal of Physiology-Lung Cellular and Molecular Physiology* 320 (2021): L715–L725.

7. R. L. Benza, M. Gomberg-Maitland, C. G. Elliott, et al., "Predicting Survival in Patients With Pulmonary Arterial Hypertension: The REVEAL Risk Score Calculator 2.0 and Comparison With ESC/ERS-Based Risk Assessment Strategies," *Chest* 156 (2019): 323–337.

8. R. L. Benza, M. K. Kanwar, A. Raina, et al., "Development and Validation of an Abridged Version of the REVEAL 2.0 Risk Score Calculator, REVEAL Lite 2, for Use in Patients With Pulmonary Arterial Hypertension," *Chest* 159 (2021): 337–346.

9. M. M. Hoeper, C. Pausch, K. M. Olsson, et al., "COMPERA 2.0: A Refined Four-Stratum Risk Assessment Model for Pulmonary Arterial Hypertension," *European Respiratory Journal* 60, Ahead of Print, July 1, 2022, https://doi.org/10.1183/13993003.02311-2021.

10. S. Hsu, C. E. Simpson, B. A. Houston, et al., "Multi-Beat Right Ventricular-Arterial Coupling Predicts Clinical Worsening in Pulmonary Arterial Hypertension," *Journal of the American Heart Association* 9 (2020): e016031.

11. M. I. Brener, A. Masoumi, V. G. Ng, et al., "Invasive Right Ventricular Pressure-Volume Analysis: Basic Principles, Clinical Applications, and Practical Recommendations," *Circulation: Heart Failure* 15 (2022): e009101.

12. B. A. Maron, G. Kovacs, A. Vaidya, et al., "Cardiopulmonary Hemodynamics in Pulmonary Hypertension and Heart Failure," *Journal of the American College of Cardiology* 76 (2020): 2671–2681.

13. M. J. Richter, D. Peters, H. A. Ghofrani, et al., "Evaluation and Prognostic Relevance of Right Ventricular–Arterial Coupling in Pulmonary Hypertension," *American Journal of Respiratory and Critical Care Medicine* 201 (2020): 116–119.

14. Right Heart Catheterisation: Best Practice and Pitfalls in Pulmonary Hypertension | European Respiratory Society, accessed May 12, 2023, https://err.ersjournals.com/content/24/138/642.

15. J. Broncano, S. Bhalla, F. R. Gutierrez, et al., "Cardiac MRI in Pulmonary Hypertension: From Magnet to Bedside," *Radiographics* 40 (2020): 982–1002.

16. L. E. R. McLure and A. J. Peacock, "Cardiac Magnetic Resonance Imaging for the Assessment of the Heart and Pulmonary Circulation in Pulmonary Hypertension," *European Respiratory Journal* 33 (2009): 1454–1466.

17. R. Inuzuka, S. Hsu, R. J. Tedford, et al., "Single-Beat Estimation of Right Ventricular Contractility and Its Coupling to Pulmonary Arterial Load in Patients With Pulmonary Hypertension," *Journal of American Heart Association* 7 (2018): e007929.

18. A. Bellofiore, R. Vanderpool, M. J. Brewis, A. J. Peacock, and N. C. Chesler, "A Novel Single-Beat Approach to Assess Right Ventricular Systolic Function," *Journal of Applied Physiology* 124 (2018): 283–290.

19. A. Schmeißer, T. Rauwolf, T. Groscheck, et al., "Predictors and Prognosis of Right Ventricular Function in Pulmonary Hypertension Due to Heart Failure With Reduced Ejection Fraction," *ESC Heart Failure* 8 (2021): 2968–2981.

20. S. Hsu, B. A. Houston, E. Tampakakis, et al., "Right Ventricular Functional Reserve in Pulmonary Arterial Hypertension," *Circulation* 133 (2016): 2413–2422.

21. P.-N. Jone, M. Schäfer, Z. Pan, and D. D. Ivy, "Right Ventricular-Arterial Coupling Ratio Derived From 3-Dimensional Echocardiography Predicts Outcomes in Pediatric Pulmonary Hypertension," *Circulation: Cardiovascular Imaging* 12 (2019): e008176.

22. M. J. Brewis, A. Bellofiore, R. R. Vanderpool, et al., "Imaging Right Ventricular Function to Predict Outcome in Pulmonary Arterial Hypertension," *International Journal of Cardiology* 218 (2016): 206–211.

23. M. Humbert, G. Kovacs, M. M. Hoeper, et al., "2022 ESC/ERS Guidelines for the Diagnosis and Treatment of Pulmonary Hypertension," *European Heart Journal* 43 (2022): 3618–3731.

24. H.-F. Yu, F.-L. Huang, and C.-J. Lin, "Dual Coordinate Descent Methods for Logistic Regression and Maximum Entropy Models," *Machine Learning* 85 (2011): 41–75.

25. A. Criminisi, "Decision Forests: A Unified Framework for Classification, Regression, Density Estimation, Manifold Learning and Semi-Supervised Learning," in *Computer Graphics and Vision*, Vol. 7 (Foundations and Trends, 2012), 81–227.

26. T. Chen and T. He, Xgboost: EXtreme Gradient Boosting.

27. A. Tharwat, "Classification Assessment Methods," *Applied Computing and Informatics* 17 (2020): 168–192.

28. T. Fawcett, "An Introduction to ROC Analysis," *Pattern Recognition Letters* 27 (2006): 861–874.

29. "Welcome to the SHAP Documentation—SHAP Latest Documentation," accessed July 24, 2023, https://shap.readthedocs.io/en/latest/index.html.

30. Z. A. Rako, N. Kremer, A. Yogeswaran, M. J. Richter, and K. Tello, "Adaptive Versus Maladaptive Right Ventricular Remodelling," *ESC Heart Failure* 10 (2023): 762–775.

31. K. Tello, J. Wan, A. Dalmer, et al., "Validation of the Tricuspid Annular Plane Systolic Excursion/Systolic Pulmonary Artery Pressure Ratio for the Assessment of Right Ventricular-Arterial Coupling in Severe Pulmonary Hypertension," *Circulation: Cardiovascular Imaging* 12 (2019): e009047.

32. A. M. Janowski, K. S. Ravellette, M. Insel, J. G. N. Garcia, F. P. Rischard, and R. R. Vanderpool, "Advanced Hemodynamic and Cluster Analysis for Identifying Novel RV Function Subphenotypes in Patients With Pulmonary Hypertension," *Journal of Heart and Lung Transplantation* 43 (2024): 755–770.

33. K. El-Kersh, C. Zhao, G. Elliott, et al., "Derivation of a Risk Score (REVEAL-ECHO) Based on Echocardiographic Parameters of Patients With Pulmonary Arterial Hypertension," *Chest* 163 (2023): 1232–1244.

34. V. Mercurio, H. J. Hassan, M. Naranjo, et al., "Risk Stratification of Patients With Pulmonary Arterial Hypertension: The Role of Echocardiography," *Journal of Clinical Medicine* 11 (2022): 4034.

35. G. D. Lewis, "Pulmonary Vascular Response Patterns to Exercise," *Advances in Pulmonary Hypertension* 9 (2010): 92–100.

36. M. J. Richter, J. Grimminger, B. Krüger, et al., "Effects of Exercise Training on Pulmonary Hemodynamics, Functional Capacity and Inflammation in Pulmonary Hypertension," *Pulmonary Circulation* 7 (2017): 20–37.

37. M. H. Lee, T. C. F. Menezes, J. A. Reisz, E. V. M. Ferreira, B. B. Graham, and R. K. F. Oliveira, "Exercise Metabolomics in Pulmonary Arterial Hypertension: Where Pulmonary Vascular Metabolism Meets Exercise Physiology," *Frontiers in Physiology* 13 (2022): 963881.

38. I. M. C. Salazar, A. C. Lancaster, V. P. Jani, et al., "Poor Cardiac Output Reserve in Pulmonary Arterial Hypertension Is Associated With

20458940, 2025, 1, Downloaded from https://onlinelibrary.wiley.com/doi/10.1002/pul2.70057, Wiley Online Library on [11/12/2025]. See the Terms and Conditions (https://onlinelibrary.wiley.com/terms-and-conditions) on Wiley Online Library for rules of use; OA articles are governed by the applicable Creative Commons License

Right Ventricular Stiffness and Impaired Interventricular Dependence," *European Respiratory Journal* 64 (2024): 2400420, https://doi.org/10.1183/13993003.00420-2024.

Supporting Information

Additional supporting information can be found online in the Supporting Information section.

20458940, 2025, 1, Downloaded from https://onlinelibrary.wiley.com/doi/10.1002/pul2.70057, Wiley Online Library on [11/12/2025]. See the Terms and Conditions (https://onlinelibrary.wiley.com/terms-and-conditions) on Wiley Online Library for rules of use; OA articles are governed by the applicable Creative Commons License